Oluwole and Olatunji
Environmental Sciences Europe (2022) 34:5
https://doi.org/10.1186/s12302-021-00588-7

Environmental Sciences Europe

RESEARCH Open Access

Photocatalytic degradation of tetracycline in aqueous systems under visible light irriadiation using needle-like SnO_2 nanoparticles anchored on exfoliated g-C_3N_4

Adewumi Olufemi Oluwole and Olatunde Stephen Olatunji*

Abstract

Background: Pharmaceuticals is one of the groups of contaminants of emerging concern that are resistant to decomposition or removal by most of the existing water and wastewater treatment procedures, hence the need to develop techniques to facilitate the removals of this group of organic contaminants from water systems. In this study, needle-like SnO_2 nanoparticles was synthesised and loaded on exfoliated g-C_3N_4 nanosheet through a hydrothermal method, for use as sensitive visible light induce-photocatalyst for the decomposition of tetracycline in aqueous systems. The synthesised composites was characterized and analysed for the nature of the heterojunction between the SnO_2 nanoparticle and g-C_3N_4 nanosheet using microscopic and spectroscopic techniques.

Results: The composites were of improved surface properties and enhanced visible-light absorption. The synthesised SnO_2/g-C_3N_4 nanocomposites with various amounts of SnO_2 (10–50 mg), employed in the degradation of tetracycline under visible light irradiation, were of good degradation efficiency. The degradation efficiencies of tetracycline by 1 wt.%, 2 wt.%, 3 wt.% and 5 wt.% SnO_2/g-C_3N_4 photocatalyst were 81.54%, 90.57%, 95.90% and 92.15% as compared to g-C_3N_4 and SnO_2 with 40.92% and 51.32% degradation efficiencies. The synergistic interaction between the needle-like SnO_2 and exfoliated g-C_3N_4 nanosheet promoted the separation of photogenerated electron holes pairs, which enhanced their migration rate between SnO2 and g-C3N4 heterojunction, thereby facilitating the degradation of tetracycline. The $\cdot O_2^-$ was noted to be the major reactive species in the photocatalytic of the 3 wt.% SnO_2/g-C_3N_4 nanocomposite.

Conclusion: The fabricated SnO_2 nanoparticles anchored on exfoliated g-C_3N_4 showed good performance for the decomposition of tetracycline in water, with possible application on other pharmaceuticals having same moiety (similar chemical structures).

Keywords: Needle-like SnO_2, SnO_2/g-C_3N_4, Nanocomposite, Tetracycline degradation, Reactive species

Introduction

Low concentrations, ranging from ng/L to µg/L of over 3000 chemicals substances, including pharmaceutical compounds (PCs), have been detected in wastewater, groundwater, surface water, soil and even in drinking water world over, for over a decade now [1–3]. The occurrence of these PCs in water bodies is due to outfalls from their global usage as therapeutic and prophylactic medicines and nutrient supplements in humans, livestocks, and agricultural health management [4–6]. The growth in population, urbanization and lifestyle places pressure on PCs demand/supply shift dynamics, resulting in increase,

*Correspondence: snf_olatunji@ymail.com
School of Chemistry and Physics, College of Agriculture, Engineering and Science, University of KwaZulu-Natal, Westville, Durban 4000, South Africa

in the production and consumption of tonnes of different pharmaceuticals in recent times.

Small to significant proprtion of pharmaceuticals administered/consumed by humans and animals are excreted from their bodies in metabolized/un-metabolized forms, and discharged via domestic wastewater into sewers and other drainage systems, from where they are transferred/translocated into freshwater surface systems and other environmental compartments. Industrial wastewater release, as well as indiscriminate disposal of unused and expired medicinal products, contributes to the total load of chemical contaminants in different environmental media [7, 8]. The environmental stability of these pharmaceutical substances (materials) coupled with the continuous unabated and uncontrollable environmental reception, has resulted in growing concerns about the potential adverse effects these compounds will have on the ecosystem and human health [9, 10].

The removal of pharmaceuticals from wastewater and other aqueous matrices, especially drinking water, is of intense focus. Unfortunately, most of the existing conventional potable water (PW) and wastewater treatment plant (WWTP) technologies encompassing biological, chemical, and adsorption processes are not designed to resolve/degrade residues of pharmaceutical compounds such as tetracycline and other antibiotics during the treatment process, prior to the release of treated water use into the environment [11]. The inability of WWTPs to eliminate many pharmaceuticals and chemical contaminants calls for the need for the development of new technologies and process designs for the degradation of these substances during water purification/treatment.

One of the possible technologies gaining traction for the resolution of pharmaceuticals and other organic contaminants in aqueous systems is the advanced oxidation procedures (AOP). AOP processes, which relies on the production of highly reactive free radicals, have proven to be a potential efficient means through which pharmaceuticals can be degraded [12, 13]. Advance oxidation procedures have been adapted in different forms ranging from ozonolysis [14], Fenton methods [15, 16], UV–Vis photo-catalysed [17], and many others. Most of these AOP adapted techniques are simple in operation; possess high catalytic activity with no selectivity for organic and inorganic compounds. They are however, limited by energy needs, non-recyclable, waste generation, incomplete decomposition and generation of solid sludge, which hinders their practical application in the degradation of pollutants within the environment [18, 19].

Oxidative degradation of pharmaceutical compounds using semiconducting photo-catalysts appears a viable option due to their simplicity, energy-saving, cheap and environmental friendliness, as well as their mild reaction condition requirements [20]. However, a major challenge arising from the use of photo-catalyst in advance oxidative photo-catalysed degradation is the narrow light response range and low quantum efficiency. It is therefore important to develop and fabricate an effective, stable and cheap visible-light-driven, efficient photocatalyst for the degradation of organic pollutants [21]. Heterostructured semiconducting nanocomposites have a promising photocatalytic activity that is amenable to tuning for improved oxidative decomposition of hazardous pollutants within an aqueous environment [22]. This is because heterostructured nanocomposites possess heterojunction properties that improve the charge transfer mechanism and slow down the fast recombination of the charge carrier. They also possess excellent physical and chemical properties that enhance the activity of active radicals during the degradation process [23]. Despite these advantages, their photocatalytic performance is hindered by the quick recombination of photoinduced charge carriers and the low surface area that limits their quantum efficiency and photocatalytic activity. The development and use of hetero-structured semiconducting nanocomposites doped on g-C3N4 is suggested as a route to address the limited visible light adsorption, and to enhance charge separation associated with many photocatalysts [24]. However, information on the use of hetero-structured nanocomposites with improved photocatalytic potentials for the oxidative degradation of pharmaceutical compounds in aqueous systems is scanty.

In this study, visible light driven needle-like SnO2/g-C3N4 photocatalyst was synthesised using a facile and economical hydrothermal method by loading various amounts of SnO2 nanosheets on exfoliated g-C3N4, characterized for phase structures, morphologies, optical properties, chemical compositions and photocatalytic performance, and tested for the oxidative photodegradation of tetracycline (TCN), an organic pollutant, under visible light irradiation. Tetracycline (TCN) is one of the commonly used broad-spectrum, cheap and readily available antibiotic pharmaceuticals. As far as we know, the degradation of tetracycline using SnO_2/g-C_3N_4 composites has not been fully explored, and very little knowledge is available concerning its use for the treatment of other pharmaceutical compounds in aqueous media.

Material and methods

Melamine (99.9%), hydrazine monohydrate (80%), ethanol, $SnCl_2.5H_2O$, benzoquinone, isopropyl alcohol, thiourea, potassium iodide, tetracycline, acetonitrile, methanol were purchased from Sigma- Aldrich, South Africa. All the reagents were of analytical grade and were used without further purification.

Preparation of thermally exfoliated g-C_3N_4 Nanosheet

The g-C_3N_4 nanosheet was synthesised by the calcination process as described by Yousaf, et al. [25] with slight modification. Briefly, 5 g of melamine was weighed into a crucible with a cover and transferred into a laboratory model muffle furnace. This was calcined at 550 °C for 4 h at a heating rate set at 10 °C/min. The resulting bulky yellow powder was allowed to cool to room temperature and thereafter crushed to a fine powder using a porcelain pestle and mortar. This resulting g-C_3N_4 fine was exfoliated by thermal treatment at 550 °C for another 2 h, at a heating rate of 10 °C/min to yield a thermal exfoliated g-C_3N_4 nanosheet.

Preparation of SnO_2/g-C_3N_4 composite photocatalysts

About 1 g of the exfoliated g-C_3N_4 nanosheet was dispersed in 120 ml of deionized water in a 250 ml beaker and ultra-sonicated for 30 min at room temperature. The sonicated g-C_3N_4 suspension was stirred continuously at room temperature for 30 min, followed by the addition of different masses of tin chloride pentahydrate (10, 20, 30, 50 mg) to different aliquots to achieve, equivalent to 1, 2, 3, 5 wt.% equivalent loadings, respectively. The resulting homogenous mixtures were stirred, thereafter, 3 ml of hydrazine hydrate was added to each of them. The resulting suspensions were stirred again for another 30 min, and then transferred into 100 ml Teflon-lined stainless-steel autoclaves and kept at 180 °C in an oven for 24 h. The autoclave was removed from the oven and allowed to cool to room temperature. The resulting precipitates of the different coupled amounts of SnO_2 nanoparticles were obtained via centrifugation, and afterwards, washed severally with deionized water and ethanol, and then dried overnight in a hot air oven at 80 °C to obtain needle-like SnO_2/g-C_3N_4. The SnO2 nanoparticles were also synthesised using the same method but without the addition of g-C3N4.

Characterization

The X-ray diffraction pattern of the prepared nanocomposites were obtained using a Shimadzu 6100 X-ray diffractometer with a CU Kα radiation source (Bruker D6).

The UV–Vis diffuse reflectance spectra (DRS) of the synthesised SnO_2/g-C_3N_4 composites were measured with Pelkin-Elmer UV–Vis spectrophotometer, the photoluminescence (PL) emissions were obtained via Perkin Elmer LS 55 spectrofluorometer.

The BET analysis (Micrometrics Tristar 3000) of the synthesised composites were carried out to determine their specific surface areas and their textural characteristics.

Their surface morphologies were also determined using the Scanning Electron Microscopy instrument (Zeiss 10 kV field). Elemental analysis of the composites were also carried out by energy dispersive spectrometry (EDS, Shimadzu), while the interfacial interaction within the synthesised composites were obtained via High-resolution transmission electron microscopy (JEOL TEM), along with the selected area electron diffraction (SAED) pattern.

The FTIR of the composites were measured on Perkin Elmer Series 100 Spectrum to determine the functional characteristics of the composites.

Electrochemical impedance spectroscopy (EIS) plots were performed by an electrochemical workstation (CHI660C, Shanghai Chenhua Instrument Corporation, China) with a three-electrode system consisting of glassy carbon electrode (GCE) as reference electrode, Pt wire as the counter electrode and ITO glass coated with SnO_2/g-C_3N_4, in an electrolyte solution made up of a mixture of 0.5 mol/L Na_2SO_4, 2.5 mmol/L potassium hexacyanoferrate (III) ($K_3[Fe(CN)_6]$), and 2.5 mmol/L potassium ferrocyanide ($K_4Fe(CN)_6 \cdot 3H_2O$).

Photocatalytic activity evaluation of the synthesised catalyst

The photocatalytic activity of the synthesised SnO_2/g-C_3N_4 composite was evaluated for the photodegradation of tetracyclines under visible light irradiation (250 W xenon lamp with a cut-off filter of 420 nm) in a photocatalytic reactor (Lelesil Innovative System, India). About 50 mg of the SnO_2/g-C_3N_4 composite materials were dispersed in 100 ml, 30 mg/L tetracycline solution. The resulting suspension of mixtures were stirred (using a magnetic stirrer) in the dark (to minimize the decomposition of tetracycline) for 30 min to attain the tetracycline—photocatalyst adsorption–desorption equilibrium. The resultant suspension solutions were exposed to continuous illumination under visible light irradiation (250 W, wavelength $\lambda = 420$ nm) for 120 min, with constant magnetic stirring to maintain cooling at temperatures between 25 and 30 °C. About 4 ml aliquots of the visible light irradiated suspensions were taken at 20 min intervals, centrifuged to remove the SnO_2/g-C_3N_4 photocatalysts, and then analysed with UV–visible spectroscopy (UV-3600-Shimadzu, UV–Vis-NIR) at an absorbance of 356 nm to determine the extent of the degradation of tetracycline.

The removal efficiency of tetracyclines by the photocatalyst was calculated as follows;

$$\text{Removal efficiency} = \frac{Co - C}{Co} \times 100\%$$

where Co is the initial concentration of tetracycline solution at time = 0 (t_0) (initial time), degradation before

treatment, while C is the concentration value at a final time after treatment.

Result and discussion

Morphology studies

The morphologies of the synthesised composites were characterised using SEM, EDX mapping, TEM, SAED, and HRTEM to confirm their crystallinity, composition, and the elemental distribution of the synthesized heterostructure composites. Figure 1(i); shows the SEM images of the exfoliated g-C_3N_4 nanosheet, SnO_2 nanoparticle and SnO_2/g-C_3N_4 heterostructure composites.

The prepared exfoliated g-C_3N_4 nanosheet are made up of lamellar structure with rough pore surfaces; the SnO_2 nanoparticles appear as tiny grain-like particles with near uniform sizes, while the morphology of the exfoliated g-C_3N_4 sheet remains unchanged. The SEM image of synthesised SnO_2/g-C_3N_4 heterostructure composites

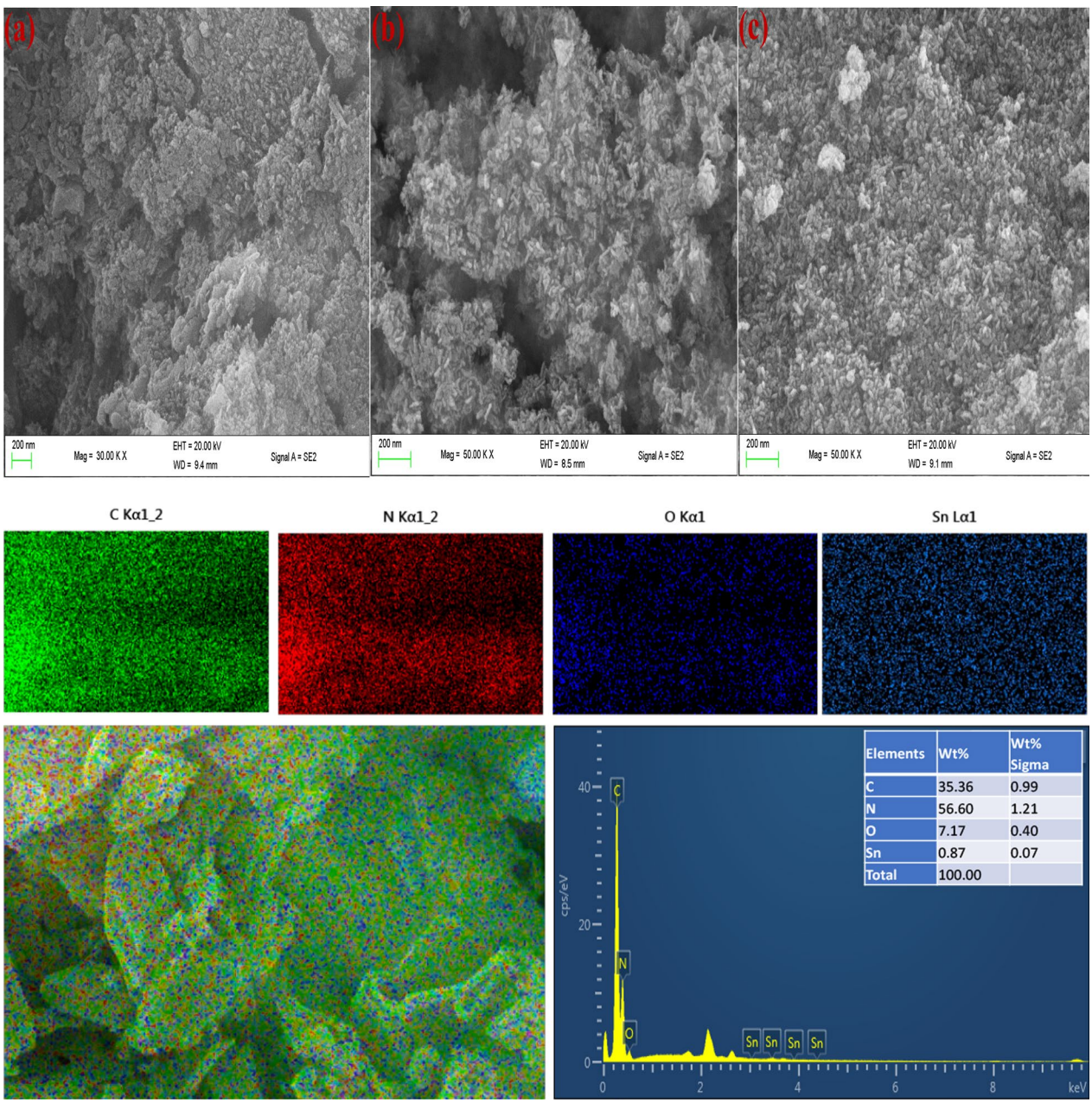

Fig. 1 (iii): TEM images of **a** g-C_3N_4 nanosheet, **b** SnO_2 nanoparticles, **c** SnO_2/g-C_3N_4 and, **d** HR-TEM image SnO_2/g-C_3N_4 composites

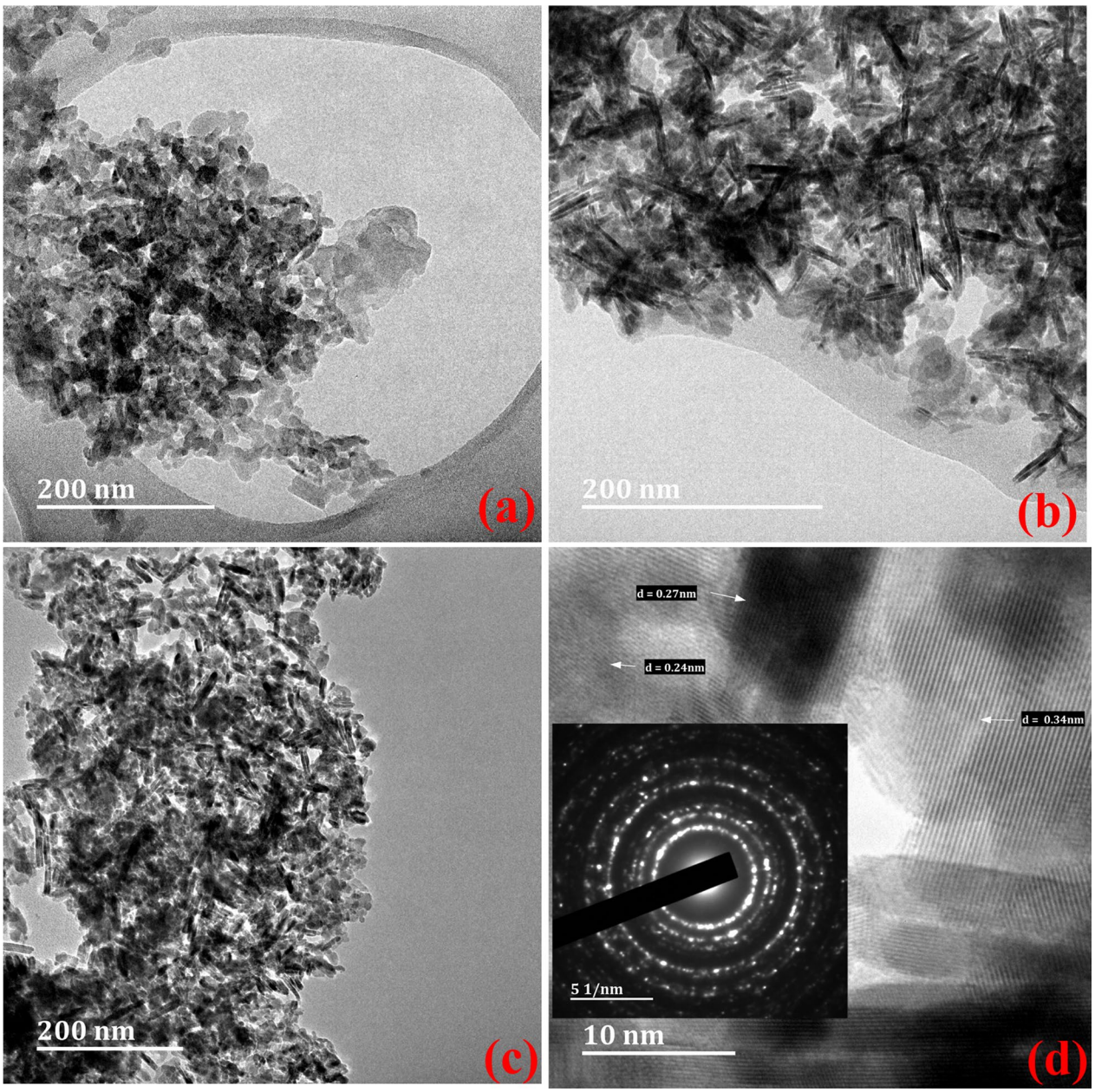

Fig. 1 continued

showed that the tiny grain-like SnO_2 were evenly decorated on the surface of the exfoliated g-C_3N_4 nanosheet, which probably partly accounts for the suppression of the recombination of photogenerated electron–hole pairs. In addition, the composites were further evaluated to confirm the presence of SnO_2 in the SnO_2/g-C_3N_4 by the EDS analysis.

The EDS of 3 wt.% SnO_2/g-C_3N_4 composites (Fig. 1(ii)), where the elements Sn, N, C and O were examined, further proved that the composites are composed of SnO_2 and g-C_3N_4. Combined with the content distribution of each element in the surface analysis and comparison with the selected area, Sn is the most abundant, covering the surface of the composites, which is indicative that SnO_2 was successfully loaded on g-C_3N_4.

The TEM micrographs of g-C_3N_4 (Fig. 1(iii)) showed a lamellar shape with several rough sheets while the synthesised needle-like SnO_2 nanoparticles were compactly and uniformly distributed on the surface of the synthesised g-C_3N_4 in the SnO_2/g-C_3N_4 composites. The

HRTEM images further confirms the deposition of SnO_2 on the surface of exfoliated g-C_3N_4 nanosheets, and the fabrication of heterostructured SnO_2/g-C_3N_4 nanocomposites (Fig. 1(iii)). The crystallographic nanoparticles lattice fringe pattern of the heterostructures SnO_2/g-C_3N_4 nanocomposites were measured to be 0.24 nm, 0.27 nm and 0.34 nm. The measured lattice fringe patterns with spacings of 0.24 nm, 0.27 nm and 0.34 nm could be respectively ascribed to the interplanar distance of (200), (101) and (110) planes of SnO_2 nanocrystals, which when combined with the XRD patterns indicates the formation of heterostructured SnO_2/g-C_3N_4 composites. Moreover, the selected area electron diffraction (SAED) pattern (Fig. 1(iii)d) displays several discrete concentric rings with superimposed bright spots, which confirms that SnO_2 are deposited on the surface of the heterostructured SnO_2/g-C_3N_4 nanocomposites. This confirms the successful formation of hybrid heterostructure between SnO_2 nanoparticles and exfoliated g-C_3N_4 nanosheet.

X-ray diffraction (XRD) analysis

The phase analysis and the crystal orientations of the synthesised SnO_2 nanoparticles, g-C_3N_4 and the corresponding needle-like SnO_2/g-C_3N_4 heterostructure composites, comprising different mass loading of SnO_2 were examined by powder X-ray diffraction (XRD). The diffraction patterns of the needle-like SnO_2 nanoparticles, g-C_3N_4 nanosheet and each of the composites were slightly variable, with those for the composites having similar 2θ diffraction (Additional file 1: Fig. S1). The major diffraction peaks in the SnO_2 nanosheet diffractogram are 26.54, 34.02, 38.03, 51.72, 54.50, 65.88 and 78.54 2θ degrees. The 2θ diffraction angles correspond to the (110), (101), (200), (211), (002), (301) and (202) crystal planes, which is consistent with the formation of pure cassiterite SnO_2 crystallite, devoid of impurities (JCPDS No 041-1445) [26]. Two significant peaks were observed on the diffractogram of the synthesised g-C_3N_4 nanosheet at 13.19 and 27.39 2θ degrees; indexed to the (002) and (100) diffraction planes assigned to the tris-s-triazine units, which is a characteristic of interlayer stacking of conjugated aromatics systems of graphitic materials (JCPDS No 87-1526) [27].

The diffractogram of the synthesized heterostructure needle-like SnO_2/g-C_3N_4 composites had two characteristic 2θ diffraction peaks at 13.02 and 27.22 2θ, attributed to the crystalline nature of g-C_3N_4 with a reduced intensity devoid of distinct diffraction peaks corresponding to the diffraction peaks of SnO_2 nanoparticles could be observed (Additional file 1: Fig. S2). This might be due to the small amount of SnO_2 contents, in the surface of exfoliated g-C_3N_4 nanosheet and their high dispersion in the interior of polymeric g-C_3N_4 nanosheet during the preparation of the nanocomposites. This is indicative that a good synergistic interaction occurs between the exfoliated g-C_3N_4 nanosheet and SnO_2 nanoparticles [28].

However, on increasing the amount of SnO_2 loaded on g-C_3N_4 from 1 wt.% and 2 wt.% to 3 wt.% and 5 wt.%, two weak peaks at 33.60° and 51.55° 2θ were observed on the XRD pattern, which were assigned to the (101) and (211) planes of tetragonal SnO_2. This is indicative that the as-synthesised photocatalyst demonstrates high crystallinity without any impurity [27, 29]. Additionally, the values of the crystallite sizes for the synthesized heterostructure composites were calculated using the Scherrer equation ($D = \frac{K\lambda}{\beta Cos\theta}$), as given [30]; where D is the crystallite size in nm, K is Scherrer's constant ≈ 0.9, λ is the wavelength of the X-ray radiation (CuKα = 0.15406 nm), β is the corrected band broadening (full width at half-maximum (FWHM)) of the diffraction peak, and θ is the diffraction angle. The particle particle size distribution of the synthesized materials generally falls within 8–23 nm (Table 1), which is indicative that they are polycrystalline in nature.

Optical characteristics: absorption and photoluminescence

The optical properties of the synthesised composites were studied to estimate their ability to absorb visible light. The bandgap of all the synthesised composites were calculated according to the Kubelka–Munk equation, $\alpha h_V = A(h_V\text{-}Eg)^{1/2}$ [31]; where α represents the adsorption coefficient; h, Planck's constant; ν, for light frequency; while *E*g and A are the bandgap energy, and constantly called band tailing parameter respectively.

The synthesised needle-like SnO_2 nanoparticles absorb in the visible light region at about 478 nm (Fig. 2). Therefore, the bandgap energy of the as-synthesised needle-like SnO_2 nanoparticles were calculated to be approximately 2.64 eV. The observed absorption and calculated bandgap may be attributed to the higher oxygen concentration due to the formation of extra ionized oxygen vacancies within the synthesised SnO_2 nanoparticles when compared to

Table 1 Specific surface area, pore volume, pore diameter and crystallite sizes of the synthesized SnO_2, g-C_3N_4 and SnO_2/g-C_3N_4 composites

Photo-catalyst	SBET (m^3/g)	Pore volume (cm^3/g)	Pore diameter (nm)	Crystallite size (nm)
SnO_2	38.06	0.057	35.50	8.73
g-C_3N_4	25.22	0.046	19.10	7.86
1% SnO_2/g-C_3N_4	27.68	0.098	23.43	19.59
2% SnO_2/g-C_3N_4	30.43	0.104	25.26	21.99
3% SnO_2/g-C_3N_4	34.37	0.137	28.62	23.50
5% SnO_2/g-C_3N_4	31.71	0.123	24.46	14.08

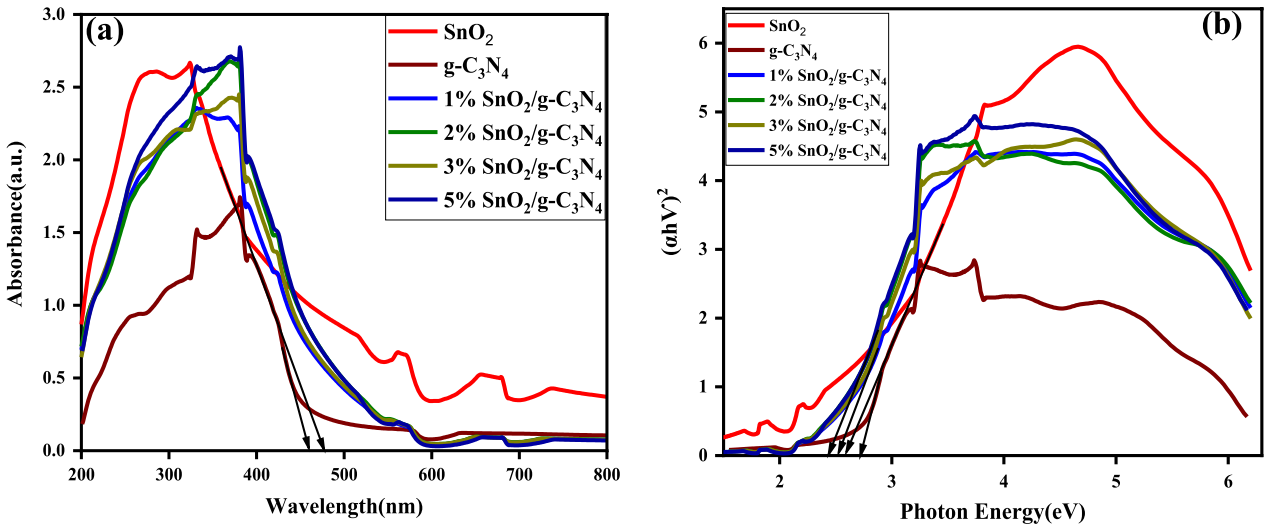

Fig. 2 **a** UV–Vis DRS and, **b** Kubelka–Munk model of SnO_2, g-C_3N_4 and its corresponding heterostructured composites

other synthesised SnO_2 with bandgap energy of about 3.60 eV [32, 33]. The g-C_3N_4 nanosheet absorbs at approximately around 458 nm, with a calculated energy bandgap of about 2.70 eV; while the energy bandgap of the synthesised composites with different weights of SnO_2 loaded on exfoliated g-C_3N_4 are close to 2.52 eV for 10% SnO_2/g-C_3N_4, and 2.45 eV for each of 2, 3, 5 wt.% SnO_2/g-C_3N_4 heterostructure composites, respectively. The calculated energy band gap values for various composites of SnO_2/g-C_3N_4 composites imply that they are photosensitive, and have the ability to respond to visible light. This also signifies that the fabrication of heterostructure composites can hinder the recombination of charge carriers, thereby causing a shift in their light response-ability towards the visible region of the spectrum. Thus, the materials synthesised SnO_2/g-C_3N_4 possess narrow bandgap, which consequently, lead to improved light harvesting capacity of the material, compared to 2.50 eV and 2.68 eV reported for the degradation of some organic pollutants [34, 35].

The photoluminescence (PL) spectra of the synthesised composites were assessed to evaluate the migration, transfer, and recombination rate of photogenerated electron–hole pairs. This is important as it helps to understand the interaction between the catalyst involved in the formation of heterojunction structure within the composites photocatalyst and the separation of the electron-holes pair, which leads to their photocatalytic activity in photodegradation application [36]. The maximum absorption wavelength used as PL excitation wavelength, was 350 nm as obtained from the UV DSR analysis. The exfoliated g-C_3N_4 nanosheets showed a strong emission peak which appears at about 425 nm (Fig. 3a). This is characteristic, for fast recombination of photogenerated charge carriers in g-C_3N_4 [37]. The observed emission bands for the synthesized needle-like SnO_2 nanoparticles were 425, 460, 484 and 532 nm (inserts in Fig. 3a). The above emission bands can be attributed to phenomenons such as crystal defects or surface defects, oxygen vacancies, tin vacancies and tin interstitials attributes in the materials [38]. Pure SnO_2 nanoparticles showed a less intense peak when compared to the intensity of the peak of the synthesised exfoliated g-C_3N_4. This suggests that the synthesized needle-like SnO_2 nanoparticles consist of a lower electron–hole recombination rate or slow recombination of photoinduced charge carriers.

Moreover, the introduction of different masses of SnO_2 nanoparticles on the exfoliated g-C_3N_4 nanosheets significantly reduced the emission peak of the exfoliated g-C_3N_4 nanosheet. The decrease in the emission intensities of the different needle-like SnO_2/g-C_3N_4 composites result from the formation of heterojunction between needle-like SnO2 nanoparticles and the g-C3N4 nanosheet, which lower electron–hole recombination or slows recombination of photoinduced charge carriers, weakened by the addition of SnO_2 nanoparticles [39]. This suggests that the synergistic interaction between SnO_2 nanoparticles and g-C_3N_4 nanosheet considerably leads to the decrease in the recombination of the photoinduced charge carrier, which is evident in its ability to degrade tetracycline under visible light.

Furthermore, electrochemical impedance spectroscopy (EIS) analysis was conducted to confirm the relevant charge transfer process and the recombination rate between the photogenerated electrons and holes. The EIS plot (Fig. 3b) reveals that the steady state perturbation in

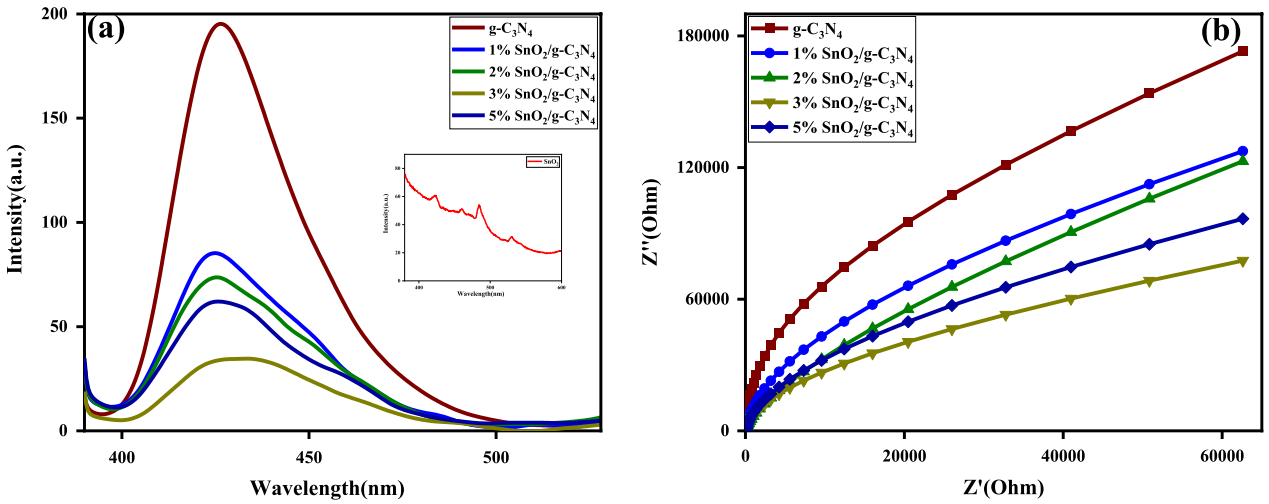

Fig. 3 **a** PL spectra of g-C_3N_4, SnO_2 and SnO_2/g-C_3N_4 composites with different compositions of SnO_2 and, **b** their corresponding EIS analysis plot

the different SnO_2/g-C_3N_4 heterostructure composites (indicated by the magnitude of the electrical impedance frequency) are much smaller than that of g-C_3N_4. This indicates that a higher charge transfer rate occurred in SnO_2/g-C_3N_4 composites, resulting in less obstruction in the transfer of electrons-holes, and thus, a more efficient separation of the charge [40]. Therefore, the % mass content of SnO_2 nanoparticles in the SnO_2/g-C_3N_4 composites clearly influences the magnitude of EI, which is consistent with the PL analysis. The 3 wt.% SnO_2/g-C_3N_4 showed lower resistance and higher separation efficiency for the photogenerated electrons and holes, thereby enhancing their potential photocatalytic efficiency for organic pollutants' degradation compared to other composites.

The FTIR spectra of the synthesised needle-like SnO_2 nanoparticles, g-C_3N_4 nanosheet and all the SnO_2/g-C_3N_4 composites were measured (Additional file 1: Fig. S3). The spectra patterns provide information and insight into the changes in the structure of the exfoliated g-C_3N_4 nanosheet. The FTIR spectrum of SnO_2 showed a broad peak around 527 cm^{-1}, characteristic of Sn–O stretching vibration of Sn–O-Sn, while the peaks at 1648 and 3362 cm^{-1} are attributed to the molecular water bending vibration and hydroxyl groups stretching vibration, respectively [39]. FTIR spectrum of g-C_3N_4 shows a peak at 804 cm^{-1} which is considered as an out-of-plane bending vibration characteristic of a tris-s-triazine ring of the g-C_3N_4 main building block. Peaks from 1204 to 1626 cm^{-1} are related to the stretching vibration modes of CN heterocycles, while the broad peak at around 3086 cm^{-1} and 3158 cm^{-1} are attributed to the stretching mode of N–H bond from the uncondensed amino groups and O–H band from absorbed water molecules [41]. The FTIR spectrum of SnO_2/g-C_3N_4 composites was made up of the main characteristic peaks of g-C_3N_4, with a slight shift in their wavenumbers, which indicates a strong interaction between exfoliated g-C_3N_4 nanosheet and SnO_2 particles.

Sorption–desorption studies

The N_2 adsorption–desorption isotherms of the synthesised composites are shown in Fig. 4. The four composites of SnO_2/g-C_3N_4 composites with the different masses of SnO_2 particles with SnO_2 and g-C_3N_4 showed type IV isotherms, while its hysteresis loops are categorized as type H3. According to the IUPAC classification, heterostructured composite materials of this type are listed as mesoporous in nature [42]. Mesoporous materials are of high surface area, and when used as photocatalyst; they have been reported to enhanced visible-light harvesting capacity vis-a-viz mesostructure light trapping in their molecules, which in turn enhances their photocatalytic efficiency by the generation of more reactive species that improves reactant adsorption for better photon-reactant molecules interactions [41].

The textural properties of the synthesised SnO_2, g-C_3N_4, and the different masses of SnO_2/g-C_3N_4 heterostructure composites such as; BET surface area, pore volume and average pore diameter are listed in Table 1. The synthesised needle-like SnO_2 nanoparticles display a high surface area of 38.06 m^3/g when compared to the synthesised exfoliated g-C_3N_4 nanosheet with surface area of 25.22 m^3/g. However, the introduction of SnO_2 into the g-C_3N_4 nanosheet results in a slight improvement in the surface area with an increase in their pore volume and

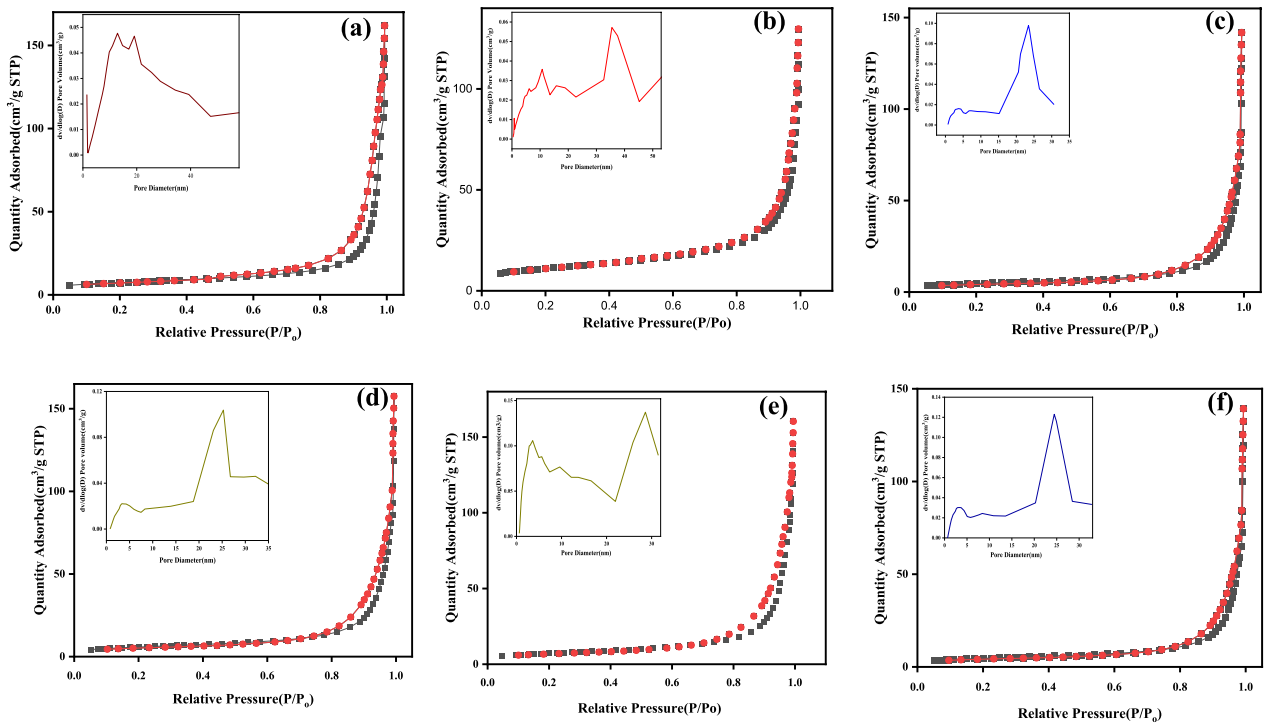

Fig. 4 N_2 adsorption of **a** g-C_3N_4, **b** SnO_2, **c** 1% SnO_2/g-C_3N_4, **d** 2% SnO_2/g-C_3N_4, **e** 3% SnO_2/g-C_3N_4, **f** 5% SnO_2/g-C_3N_4 **g** and with their respective pore size distribution plot inserted

pore diameter of the different composites. The 3 wt.% SnO_2/g-C_3N_4 composites showed the best textural properties of 34.37 m^3/g, 0.137 cm^3/g, 28.62 nm for it's surface area, pore volume and pore diameter, respectively. The improvement in the surface area of the composites indicates that some changes occurred during the incorporation of SnO_2 on g-C_3N_4, which could facilitate the transfer of photoinduced electron–hole pairs, hence, improving their photocatalytic efficiency for the degradation of organic pollutants.

Thermogravimetric (TGA) analysis

The thermal stability of the synthesised materials were analysed by thermogravimetric analysis in an atmosphere of air at a heating rate of 10.00 °C/min. An initial weight loss at the temperature of 50–200 °C was observed for all materials (Additional file 1: Fig. S4a). This can be attributed to the loss of absorbed water and other substances on the surface of the materials [43]. The gradual weight loss for g-C_3N_4 after 550 °C may be associated with the combustion of the carbon skeleton and the decomposition of defects and edge functional groups like uncondensed amine functional groups and the edge cyano-group that exist within g-C_3N_4 nanosheet [44]. Meanwhile, the weight loss of the different masses of SnO_2 nanoparticle loaded on the g-C_3N_4 sheet between the temperature range of 400 and 550 °C may be ascribed to the combustible carbon and the decomposition of the functional groups in the g-C_3N_4 structure, while the SnO_2 nanoparticle maintains its stability with a nearly straight line [45]. The specific decomposition temperatures of the synthesised materials are 703 °C, 658 °C, 635 °C with 50% SnO_2/g-C_3N_4 showing the lowest stability at 595 °C, while the g-C_3N_4 nanosheet shows the highest stability of 720 °C (Additional file 1: Fig. S4b). The TGA revealed that the synthesised materials are thermally stable, while its composition are consistent with the original materials.

Photocatalytic evaluation

The photocatalytic activity of the composites with different needle-like SnO_2 nanoparticles mass loads on exfoliated g-C_3N_4 nanosheets for the photocatalytic degradation of tetracycline under visible light irradiation the effects of SnO_2 mass loads was investigated. The visible light-assisted degradation of tetracycline in reaction systems in which the different synthesised composites were dispersed and dark stabilised for 30 min to attain adsorption–desorption equilibrium prior to visible light exposure were fairly. The exposure of the tetracycline solution to visible light irradiation caused minimum degradation of about 26.90%, while a 40.92% and 51.32% degradation was observed when exfoliated g-C_3N_4 nanosheet and

needle-like SnO_2 were added to the tetracycline solution as a catalyst, respectively, after 120 min (Fig. 5a).

The concentration of tetracycline decreased significantly when the different composites SnO_2/g-C_3N_4 were used as catalysts. The degradation efficiencies of tetracycline by the 1 wt.%, 2 wt.%, 3 wt.% and 5 wt.% SnO_2/g-C_3N_4 photocatalyst were 81.54%, 90.57%, 95.90% and 92.15%, respectively. It is important to note that the photocatalytic ability of the different SnO_2/g-C_3N_4 composites increased with respect to the amount of SnO_2 nanoparticles added to the g-C_3N_4 nanosheet until 3 wt.% SnO_2/g-C_3N_4 composite, which displayed the highest degradation of 95.90% tetracycline degradation within 120 min irradiation under visible light, after which a decrease was observed with increase in % wt. SnO_2 load. This implies that an increase in the content of SnO2 in the SnO2/g-C3N4 composites plays an important role in catalysing the degradation of tetracycline molecules vis-a-viz the formation of heterojunction within the structural configuration of the SnO_2/gC_3N_4 composites. The heterostructured characteristics of the SnO_2/gC_3N_4 play a crucial role in improving the photocatalytic activity of the composites. Hence, the photocatalytic efficiency can be optimized by adjusting the content of SnO_2 nanoparticles on exfoliated g-C_3N_4 nanosheet.

More also, the efficiently high tetracycline degradation of 95.90% by the 30% SnO_2/g-C_3N_4 composite could be because of their promoted charge separation, which results in increased quantum confinement leading and low recombination of photogenerated charge, as well as its larger surface area when compared to other composites (Table 1). On the other hand, increasing the SnO_2 composite content to 5 wt.% in the SnO_2/g-C_3N_4 led to a decrease in the photocatalytic activity. This may be due to the shielding of the active sites as a result of the excess addition of SnO_2 on the exfoliated g-C_3N_4 nanosheet, which in turn hinders the light-capturing capacity of g-C_3N_4 under visible light irradiation during the photodegradation process [46].

The photocatalytic kinetics for the degradation of tetracycline was studied. The degradation process obeyed the pseudo-first order kinetics model ($-In(\frac{C}{Co}) = kt$); where k represents the reaction rate constant while Co and C stand for the initial concentration and final concentration of tetracycline at time t, respectively.

The calculated rate constant (k) and the mean regression coefficients (R^2) values for the kinetics of the degradation of tetracycline with different amounts of SnO_2 nanoparticles loaded on the g-C_3N_4 sheets are presented in Fig. 5b. The calculated k values are 0.0062, 0.00671, 0.0107, 0.0215, 0.0235 and 0.0222 min^{-1} for 1 wt.%, 2 wt.%, 3 wt.% and 5 wt.% SnO2QDs/g-C3N4, respectively (Table 2). The as-synthesised 3 wt.% SnO_2/g-C_3N_4 nanocomposites exhibited a superior k value when compared to the other nanocomposites, generating a rate constant that is 6.32 and 4.33 times better than those of pure g-C_3N_4 nanosheet and SnO_2 nanoparticle, respectively, for the degradation of tetracycline. This showed that loading different amounts of SnO_2 on g-C_3N_4 can improve the degradation of tetracycline under visible light. This can be attributed to a decrease in the recombination of the electron–hole pairs through the formation of localized states between the conduction and valence bands.

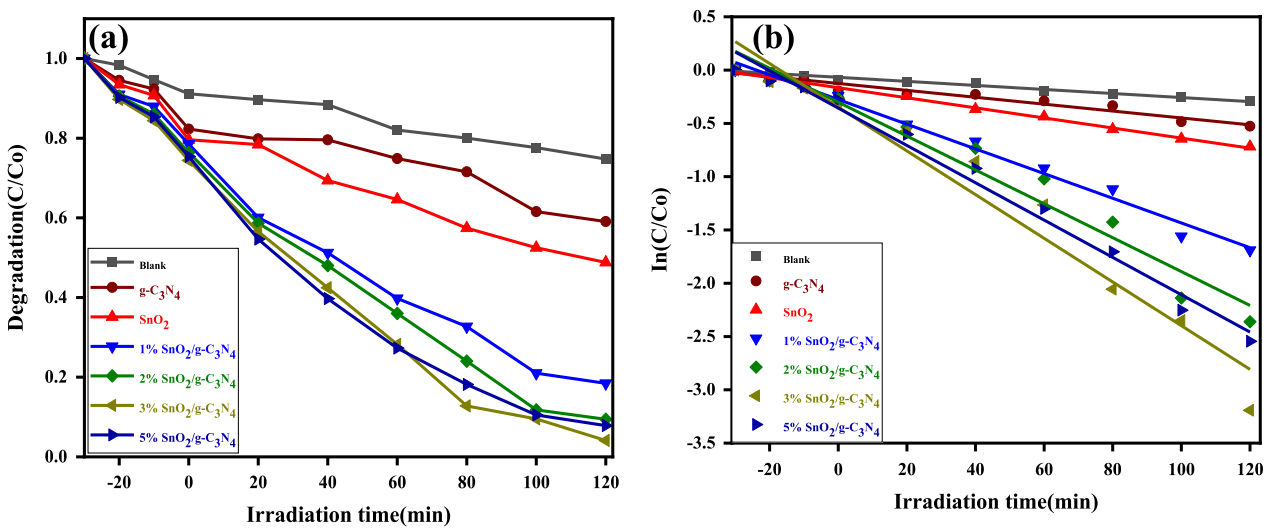

Fig. 5 **a** photocatalytic activities of the synthesized composite, **b** kinetics studies

Table 2. Summary of photocatalytic degradation of tetracycline visible light irradiation using SnO_2/g-C_3N_4 heterostructured composites

Photo-catalyst	Degradation (%)	Rate constant, K (min^{-1})	R^2
Blank	25.23	0.00190	0.9816
SnO_2	40.92	0.00324	0.9537
g-C_3N_4	51.20	0.00473	0.9895
1% SnO_2/g-C_3N_4	81.54	0.0115	0.9879
2% SnO_2/g-C_3N_4	90.57	0.0159	0.9609
3% SnO_2/g-C_3N_4	95.90	0.0205	0.9553
5% SnO_2/g-C_3N_4	92.15	0.0175	0.9832

Photocatalyst reusability

Recyclability and stability are among the important parameters considered in the practicality of a photocatalyst. This was evaluated for the practical application of the synthesised SnO_2/g-C_3N_4 heterostructured composites in five cycling experiments, for the degradation of tetracycline under the same reaction condition (50 mg of the catalyst dispersed in 100 ml, 30 mg/L tetracycline solution). At the end of each reaction cycle, the spent solutions were centrifuged to recover the SnO_2/g-C_3N_4 composites used as catalysts and washed severally with water and ethanol, followed by overnight drying in the oven at 80 °C. About 86.78% of the tetracycline was degraded on the fifth run after 120 min, showing a slight reduction in the photocatalytic efficiency of 3 wt.% SnO_2/g-C_3N_4 compared to the first run which had 95.90% degradation, under the same photocatalytic condition (Additional file 1: Fig. S5). This might be due to the loss of the photocatalyst charge during the recycling process.

Furthermore, the crystal structure of the 3 wt.% SnO_2/g-C_3N_4 composite photocatalyst was investigated prior to- and after use in five-cycle experiments of the photocatalytic process, to evaluate and confirm whether there was any distortion or changed in the crystal structure, using XRD analysis. The results showed that there was no significant change in their crystalline structure, thus suggesting that the chemical structures of the photocatalysts were not affected after use, hence their stability. It can therefore be inferred that the 3 wt.% SnO_2/g-C_3N_4 displayed high stability under visible light for the degradation of tetracycline, probably because of the π-π stacking interaction that exists between the photocatalyst and the tested pollutants [47].

To understand the photocatalytic mechanisms and elucidate the reactive species involved during the photocatalytic degradation of tetracycline using 3 wt.% SnO_2/g-C_3N_4 heterostructured composite under visible light irradiation, various scavengers such as potassium iodide KI for H^+ scavenging, p-benzoquinone (PBQ) for $^{\cdot\cdot}O_2^-$, Isopropyl alcohol (IPA) for $^{\cdot\cdot}OH$ scavenging and lastly thiourea for scavenging $OH^{\cdot\cdot}$, H^+ and e^- were used as suggested by Bui, et al. [48]. The same experimental procedure for the photocatalytic activity were used. Results revealed that the introduction of thiourea into the reaction medium led to a considerable decrease in tetracycline degradation (65.54%); KI addition led to 87.62% removal efficiency, PBQ caused 56.41 removals. However, the addition of IPA significantly suppresses tetracycline degradation by 41.38% when compared to degradation without scavenger (Additional file 1: Fig. S6). These results indicate that the presence of •OH and $\bullet O_2^-$ radical proved to be the major reactive species for the degradation of tetracycline using 3 wt.% SnO_2/g-C_3N_4 as photo-catalyst.

The calculated conduction band (CB) and valence band (VB) of SnO_2 are 3.04 eV and 0.40 eV while that of g-C_3N_4 nanosheet are −1.12 eV and 1.58 eV, respectively; showing that the compositing semiconductors have suitable band potentials that led to the formation of heterojunction structures to restrain the recombination of electron-holes pairs. Based on the characterisation and experimental data obtained in this study, a tentative mechanism for the photodegradation of tetracycline using SnO_2/g-C_3N_4 composites under visible light irradiation is proposed (Additional file 1: Fig. S7). Upon reception of visible light irradiation on the composites, both g-C_3N_4 and SnO_2 generated electrons and holes, leading to te migration of the photoexcited electrons from the CB of g-C_3N_4 nanosheet to the CB of SnO_2 nanoparticles. In contrast, the photoexcited holes migrates from the VB of g-C_3N_4 to the VB of SnO_2 resulting in the effective separation of the photoexcited charge carriers, which enhances their photocatalytic performance for the degradation of tetracycline under visible light irradiation.

From the Mott-Schottky plot, as shown in Additional file 1: Fig. S8, the flat band potential for the g-C_3N_4, SnO_2 and the 3 wt.% SnO_2/g-C_3N_4 composites were estimated to be −1.33, −0.12 and −1.15 eV. Generally, the conduction band potential of a semiconductor is −0.1 or −0.2 eV, more negative than the flat band potential. Therefore the estimated conductor band from the recorded flat band potentials are −1.43, −0.22, −1.25 eV. Moreover, the valence band potential of g-C_3N_4, SnO_2 and SnO_2/g-C_3N_4 were calculated (1.27, 2.42 and 1.20 eV) using the Butler and Ginley equations [49] as given in Eqs. 1 and 2:

$$E_{VB} = \chi - E^e + 0.5E_g \quad (1)$$

$$E_{CB} = E_{VB} - E_g \quad (2)$$

where the value of E^c is 4.5 eV, X value of SnO_2 is 6.22 eV, while that of g-C_3N_4 is 4.73 eV which was similar to the values reported by Sun et al. [50]. The bandgap energy (Eg) of g-C_3N_4 and SnO_2 as obtained from UV–Vis DRS are 2.70 eV and 2.64 eV.

The electronic structure of the composites was influenced by the large percentage composition of g-C_3N_4 being the base material, while the small quantity of SnO_2 in the composites led to the suppression of its electronic structure. From the above discussion, it is evident that the conduction band potential of the composites is higher than the required electron reduction potential (−0.33) for the conversion of an oxygen molecule to superoxide anions radicals. Hence the reason superoxide anion radical is the determining oxygen species for the photocatalytic degradation of tetracycline. On the other hand, the valence band (1.20 eV) is less positive than the required oxidative potential for the conversion of H_2O molecule and OH^- ions to hydroxyl radicals (HO•) which explains the insufficient amount of hydroxyl radicals in the system. Moreover, the conduction band position of g-C_3N_4 nanosheet is −1.12 eV vs. NHE, which is more negative than that of SnO_2 nanoparticle (0.04 eV vs. NHE) with a redox potential of $O_2/•O_2^-$ (+0.28 eV vs NHE). This shows that the photogenerated electrons could react with the adsorbed O_2 to produce active oxygen species $•O_2^-$ radicals.

Conclusions

Series of visible light-driven SnO_2/g-C_3N_4 heterostructure composites were synthesised via a facile hydrothermal method. The loading of different masses of SnO_2 nanoparticles on the synthesised exfoliated g-C_3N_4 sheets produces a strong heterojunction and improved specific surface area coupled with good optical properties. As revealed by the SEM, TEM and HR-TEM the synthesised composites generated a needle-like crystal structure with the uniform distribution of the SnO_2 nanoparticles on the surface of the g-C_3N_4 nanosheet while the PL result confirm the decrease in the recombination rate due to the introduction of SnO_2 nanoparticle on to the surface of the exfoliated g-C_3N_4 sheet. After comparison, 3 wt.% SnO_2/g-C_3N_4 composites exhibited a higher photocatalytic performance than other composites as a result of improved specific surface area and charge separation efficiency. From the photocatalytic analysis, it was observed that the $•O_2^-$ and •OH, radicals are the main active species generated during the photocatalysis process due to the action of electron reduction.

Moreover, the kinetic rate constant, recyclability and stability of the synthesised composites for the degradation of tetracycline were also analysed with obtained results showing excellent capability and robustness of the composites towards the degradation of tetracycline under visible light irradiation. The heterostructure composite mechanism pathway for the degradation of tetracycline under visible light irradiation were also proposed. Attributable to the improved performances of the synthesised composites for visible-light responsive applications, materials with such efficiency have potential environmental applications.

Supplementary Information

The online version contains supplementary material available at https://doi.org/10.1186/s12302-021-00588-7.

Additional file 1: Fig. S1. XRD patterns of (a) SnO_2 nanoparticles, (b) g-C_3N_4 nanosheet and, (c) different mass combinations of SnO_2/g-C_3N_4 heterostructure composites. **Fig. S2.** Diffractograms of synthesized heterostructure needle-like SnO_2/g-C_3N_4 composites devoid of distinct diffraction peaks of SnO_2 nanoparticles. **Fig. S3.** FTIR Spectra of pure SnO_2, g-C_3N_4, and SnO_2/g-C_3N_4 composites. **Fig. S4.** (a) TGA thermograms and (b) the corresponding derivative thermograms of the synthesized heterostructured composites. **Fig. S5.** (a) recyclability test of 30% SnO_2/g-C3N4 composite and (b) XRD pattern of 30%SnO_2/g-C_3N_4 before photoreaction and used after five repeated cycles of photodegradation experiments. **Fig. S6.** showing the effects of various scavengers on the tetracycline degradation using 3% SnO_2/g-C_3N_4 under visible light irradiation. **Fig. S7.** Reaction mechanism pathway for the degradation of tetracycline through 30% SnO_2/g-C_3N_4. **Fig. S8.** Mott-Schottky plots measured at 1 kHz in 5 mM $[Fe(CN)6]^{4-/3-}$ solution.

Acknowledgements
Not applicable.

Authors' contributions
AO and OO contributed equally to this work. Both authors read and approved the final manuscript.

Funding
Not applicable.

Availability of data and materials
The data sets used and/or analyzed during the current study are available from the corresponding author on reasonable request.

Declarations

Ethics approval and consent to participate
Not applicable.

Consent for publication
Not applicable.

Competing interests
The authors wish to state that there was no conflict of interest.

Received: 29 October 2021 Accepted: 28 December 2021
Published online: 10 January 2022

References

1. He K, Borthwick AG, Lin Y, Li Y, Fu J, Wong Y, Liu W (2020) Sale-based estimation of pharmaceutical concentrations and associated environmental risk in the Japanese wastewater system. Environ Int 139:105690
2. Zhou S, Di Paolo C, Wu X, Shao Y, Seiler T-B, Hollert H (2019) Optimization of screening-level risk assessment and priority selection of emerging

pollutants–The case of pharmaceuticals in European surface waters. Environ Int 128:1–10
3. Ebele AJ, Oluseyi T, Drage DS, Harrad S (2020) Occurrence, seasonal variation and human exposure to pharmaceuticals and personal care products in surface water, groundwater and drinking water in Lagos State, Nigeria. Emerg Contam 6:124–132
4. der Beek T, Weber FA, Bergmann A, Hickmann S, Ebert I, Hein A, Küster A (2016) Pharmaceuticals in the environment—Global occurrences and perspectives. J Environ Toxicol Chem 35(4):823–835
5. Ebele AJ, Abdallah MAE, Harrad S (2017) Pharmaceuticals and personal care products (PPCPs) in the freshwater aquatic environment. J Emerg Contam 3(1):1–16
6. Starling MCV, Amorim CC, Leão MMD (2019) Occurrence, control and fate of contaminants of emerging concern in environmental compartments in Brazil. J Hazard Mater 372:17–36
7. Boxall AB, Sinclair CJ, Fenner K, Kolpin D, Maund SJ (2004) Peer reviewed: when synthetic chemicals degrade in the environment. ACS Publications, In.
8. Huerta B, Rodriguez-Mozaz S, Nannou C, Nakis L, Ruhí A, Acuña V, Sabater S, Barcelo D (2016) Determination of a broad spectrum of pharmaceuticals and endocrine disruptors in biofilm from a waste water treatment plant-impacted river. Sci Total Environ 540:241–249
9. Margiotta-Casaluci L, Owen SF, Cumming RI, de Polo A, Winter MJ, Panter GH, Rand-Weaver M, Sumpter JP (2014) Quantitative cross-species extrapolation between humans and fish: the case of the anti-depressant fluoxetine. PLoS ONE 9:10
10. Sun H, Wang T, Yang Z, Yu C, Wu W (2019) Simultaneous removal of nitrogen and pharmaceutical and personal care products from the effluent of waste water treatment plants using aerated solid-phase denitrification system. Bioresource Technol 287:121389
11. Varma KS, Tayade RJ, Shah KJ, Joshi PA, Shukla AD, Gandhi VG (2020) Photocatalytic degradation of pharmaceutical and pesticide compounds (PPCs) using doped TiO_2 nanomaterials: a review. Water-Energy Nexus 3:46–61
12. Ahmadi M, Motlagh HR, Jaafarzadeh N, Mostoufi A, Saeedi R, Barzegar G, Jorfi S (2017) Enhanced photocatalytic degradation of tetracycline and real pharmaceutical wastewater using MWCNT/TiO_2 nanocomposite. J Environ Manage 186:55–63
13. Lin L, Wang H, Xu P (2017) Immobilized TiO_2-reduced graphene oxide nanocomposites on optical fibers as high performance photocatalysts for degradation of pharmaceuticals. Chem Eng J 310:389–398
14. Ren D, Diao E, Hou H, Dong H (2020) Degradation and ozonolysis pathway elucidation of deoxynivalenol. Toxicon 174:13–18
15. Li X, Cui K, Guo Z, Yang T, Cao Y, Xiang Y, Chen H, Xi M (2020) Heterogeneous Fenton-like degradation of tetracyclines using porous magnetic chitosan microspheres as an efficient catalyst compared with two preparation methods. Chem Eng J 379:122324
16. Zhuang Y, Wang X, Liu Q, Shi B (2020) N-doped FeOOH/RGO hydrogels with a dual-reaction-center for enhanced catalytic removal of organic pollutants. Chem Eng J 379:122310
17. Luu HT, Lee K (2014) Degradation and changes in toxicity and biodegradability of tetracycline during ozone/ultraviolet-based advanced oxidation. Water Sci Technol 70(7):1229–1235
18. Yu M, Wang J, Tang L, Feng C, Liu H, Zhang H, Peng B, Chen Z, Xie Q (2020) Intimate coupling of photocatalysis and biodegradation for wastewater treatment: Mechanisms, recent advances and environmental applications. Water Res 1:115673
19. Al-Mamun M, Kader S, Islam M, Khan M (2019) Photocatalytic activity improvement and application of UV-TiO_2 photocatalysis in textile wastewater treatment: a review. J Environ Chem Eng 7(5):103248
20. Nasr O, Mohamed O, Al-Shirbini A-S, Abdel-Wahab A-M (2019) Photocatalytic degradation of acetaminophen over Ag, Au and Pt loaded TiO_2 using solar light. J Photochem Photobiol, A 374:185–193
21. Chu L, Duo F, Zhang M, Wu Z, Sun Y, Wang C, Dong S, Sun J (2020) Doping induced enhanced photocatalytic performance of SnO_2: Bi^{3+} quantum dots toward organic pollutants. Colloids Surf A 1:124416
22. Masjedi-Arani M, Salavati-Niasari M (2017) Metal (Mn Co, Ni and Cu) doped ZnO-Zn2SnO4-SnO2 nanocomposites: Green sol-gel synthesis, characterizationand photocatalytic activity. J Mol Liq 248:197–204
23. Gómez-Pastora J, Dominguez S, Bringas E, Rivero MJ, Ortiz I, Dionysiou DD (2017) Review and perspectives on the use of magnetic nanophotocatalysts (MNPCs) in water treatment. Chem Eng J 310:407–427
24. Ismael M (2020) The photocatalytic performance of the ZnO/g-C_3N_4 composite photocatalyst toward degradation of organic pollutants and its inactivity toward hydrogen evolution: The influence of light irradiation and charge transfer. Chem Phys Lett 739:136992
25. Yousaf MU, Pervaiz E, Minallah S, Afzal MJ, Honghong L, Yang M (2019) Tin oxide quantum dots decorated graphitic carbon nitride for enhanced removal of organic components from water: Green process. Results Phys 14:102455
26. Zhang H, Xu P, Ni Y, Geng H, Zheng G, Dong B, Jiao Z (2014) In situ chemical synthesis of SnO_2/reduced graphene oxide nanocomposites as anode materials for lithium-ion batteries. J Mater Res 29(5):617–624
27. Zou Y, Xie Y, Yu S, Chen L, Cui W, Dong F, Zhou Y (2019) SnO_2 quantum dots anchored on g-C_3N_4 for enhanced visible-light photocatalytic removal of NO and toxic NO_2 inhibition. Appl Surf Sci 496:143630
28. Liu H, Du C, Li M, Zhang S, Bai H, Yang L, Zhang S (2018) One-pot hydrothermal synthesis of SnO_2/BiOBr heterojunction photocatalysts for the efficient degradation of organic pollutants under visible light. ACS Appl Mater Interfaces 10(34):28686–28694
29. Yang L, Huang J, Shi L, Cao L, Zhou W, Chang K, Meng X, Liu G, Jie Y, Ye J (2017) Efficient hydrogen evolution over Sb doped SnO_2 photocatalyst sensitized by Eosin Y under visible light irradiation. Nano Energy 36:331–340
30. Kaur H, Bhatti H, Singh K (2019) Dopant incorporation in ultrasmall quantum dots: a case study on the effect of dopant concentration on lattice and properties of SnO_2 QDs. J Mater Sci: Mater Electron 30(3):2246–2264
31. Yuan Y, Huang G-F, Hu W-Y, Xiong D-N, Zhou B-X, Chang S, Huang W-Q (2017) Construction of g-C_3N_4/CeO_2/ZnO ternary photocatalysts with enhanced photocatalytic performance. J Phys Chem Solids 106:1–9
32. Han X, Zhao J, An L, Li Z, Xin Y (2019) One-step synthesis of oxygen vacancy-rich SnO_2 quantum dots with ultrahigh visible-light photocatalytic activity. Mater Res Bull 118:110486
33. Babu B, Shim J, Yoo K (2020) Effects of annealing on bandgap and surface plasmon resonance enhancement in Au/SnO_2 quantum dots. Ceram Int 46(1):17–22
34. Chu C, Miao W, Li Q, Wang D, Liu Y, Mao S (2022) Highly efficient photocatalytic H_2O_2 production with cyano and SnO_2 co-modified g-C_3N_4. Chem Eng J 132531
35. Nguyen-Dinh M-T, Bui TS, Bansal P, Jourshabani M, Lee B-K (2021) Photocatalytic and photo-electrochemical behavior of novel SnO_2-modified-g-C_3N_4 for complete elimination of tetracycline under visible-light irradiation: Slurry and fixed-bed approach. Separ Purif Technol 267:118607
36. Lin X, Huang F, Xing J, Wang W, Xu F (2008) Heterojunction semiconductor SnO_2/$SrNb_2O_6$ with an enhanced photocatalytic activity: The significance of chemically bonded interface. Acta Mater 56(12):2699–2705
37. Chuang P-K, Wu K-H, Yeh T-F, Teng H (2016) Extending the π-conjugation of g-C_3N_4 by incorporating aromatic carbon for photocatalytic H_2 evolution from aqueous solution. ACS Sustain Chem Eng 4(11):5989–5997
38. Luo S, Wan Q, Liu W, Zhang M, Song Z, Lin C, Chu PK (2005) Photoluminescence properties of SnO_2 nanowhiskers grown by thermal evaporation. Prog Solid State Chem 33(2–4):287–292
39. Jingyu H, Ran Y, Zhaohui L, Yuanqiang S, Lingbo Q, Kani AN (2019) In-situ growth of ZnO globular on g-C_3N_4 to fabrication binary heterojunctions and their photocatalytic degradation activity on tetracyclines. Solid State Sci 92:60–67
40. Di J, Xia J, Ge Y, Xu L, Xu H, Chen J, He M, Li H (2014) Facile fabrication and enhanced visible light photocatalytic activity of few-layer MoS_2 coupled BiOBr microspheres. Dalton Trans 43(41):15429–15438
41. Jourshabani M, Shariatinia Z, Badiei A (2017) Sulfur-doped mesoporous carbon nitride decorated with Cu particles for efficient photocatalytic degradation under visible-light irradiation. J Phys Chem C 121(35):19239–19253
42. Sing KS (1985) Reporting physisorption data for gas/solid systems with special reference to the determination of surface area and porosity (Recommendations 1984). Pure Appl Chem 57(4):603–619
43. Chen Y, Wang B, Lin S, Zhang Y, Wang X (2014) Activation of n→ π* transitions in two-dimensional conjugated polymers for visible light photocatalysis. J Phys Chem C 118(51):29981–29989

44. Yao Y, Lu F, Zhu Y, Wei F, Liu X, Lian C, Wang S (2015) Magnetic core–shell $CuFe_2O_4$@C_3N_4 hybrids for visible light photocatalysis of Orange II. J Hazard Mater 297:224–233
45. Liu J, Wang L, Wang J, Zhang L (2013) Simple solvothermal synthesis of hydrophobic magnetic monodispersed Fe_3O_4 nanoparticles. Mater Res Bull 48(2):416–421
46. Chang C, Fu Y, Hu M, Wang C, Shan G, Zhu L (2013) Photodegradation of bisphenol A by highly stable palladium-doped mesoporous graphite carbon nitride (Pd/mpg-C_3N_4) under simulated solar light irradiation. Appl Catal B 142:553–560
47. Wang X, Ren P (2018) Flower-like SnO_2/g-C_3N_4 heterojunctions: the face-to-face contact interface and improved photocatalytic properties. Adv Powder Technol 29(5):1153–1157
48. Bui TS, Bansal P, Lee B-K, Mahvelati-Shamsabadi T, Soltani T (2020) Facile fabrication of novel Ba-doped g-C_3N_4 photocatalyst with remarkably enhanced photocatalytic activity towards tetracycline elimination under visible-light irradiation. Appl Surf Sci 506:144184
49. Chen G, Bian S, Guo C-Y, Wu X (2019) Insight into the Z-scheme heterostructure WO_3/g-C_3N_4 for enhanced photocatalytic degradation of methyl orange. Mater Lett 236:596–599
50. Sun H, Zhou G, Wang Y, Suvorova A, Wang S (2014) A new metal-free carbon hybrid for enhanced photocatalysis. ACS Appl Mater Interfaces 6(19):16745–16754

Publisher's Note